

Physical Properties of Trans-Neptunian Object (20000) Varuna

David C. Jewitt and Scott S. Sheppard

Institute for Astronomy, University of Hawaii,

2680 Woodlawn Drive, Honolulu, HI 96822

jewitt@ifa.hawaii.edu, sheppard@ifa.hawaii.edu

Received _____; accepted _____

arXiv:astro-ph/0201082v1 7 Jan 2002

ABSTRACT

We present new time-resolved photometric observations of the bright trans-Neptunian object (20000) Varuna and use them to study the rotation period, shape, and color. In observations from 2001 February and April, we find a best-fit two-peaked lightcurve with period 6.3442 ± 0.0002 hr. The peak-to-peak photometric range in the R-band is 0.42 ± 0.02 mag. We find no rotational variation in colors over the $0.45 \leq \lambda \leq 0.85\mu\text{m}$ wavelength range. From the short double-peaked period and large amplitude we suggest that Varuna is an elongated, prolate body perhaps close in shape to one of the Jacobi ellipsoids. If so, the ratio of the axes projected into the plane of the sky is 1.5:1 and the density is near 1000 kg m^{-3} . (20000) Varuna may be a rotationally distorted rubble pile, with a weak internal constitution due to fracturing by past impacts. The high specific angular momentum implied by our observations and recent detections of binary Trans-Neptunian Objects both point to an early, intense collisional epoch in which large Trans-Neptunian Objects were ~ 100 times more abundant than now. In order to maintain a cosmochemically plausible rock:ice mass ratio ~ 0.5 , Varuna must be internally porous.

Subject headings: Kuiper Belt, Oort Cloud - minor planets, solar system: general

1. Introduction

The trans-Neptunian objects (TNOs) have semi-major axes larger than that of Neptune (Jewitt and Luu 2000) and are thought to be the products of arrested growth in the tenuous outer parts of the accretion disk of the sun (Kenyon and Luu 1999). Their large mean heliocentric distances and resulting low surface temperatures suggest that they may retain a substantial volatile fraction. Indeed, the trans-Neptunian region is widely held to be the source of the ice-rich nuclei of short period (specifically Jupiter-family) comets. In this sense, the TNOs are repositories of some of the solar system’s least evolved, most primitive material. There is widespread interest in the physical (and chemical) properties of these bodies. Unfortunately, most known TNOs are too faint to permit easy investigation even when using the largest available telescopes. For this reason, the bright TNO (20000) Varuna (apparent red magnitude ~ 19.7) has already attracted considerable observational attention.

Varuna was discovered on 2000 November 28 and given the provisional designation 2000 WR106 (McMillan and Larsen 2000). Prediscovery observations from 1955 were soon uncovered (Knofel and Stoss 2000), leading to the accurate determination of the orbit and the classification as a ”classical TNO” (Jewitt and Luu 2000), with semimajor axis 43.274 AU, inclination 17.1° and eccentricity 0.056. Simultaneous thermal and optical observations give red geometric albedo $p_R = 0.07^{+0.030}/_{-0.017}$ and equivalent circular diameter $900^{+129}/_{-145}$ km (Jewitt, Aussel and Evans 2001). Varuna is currently one of the biggest known Trans-Neptunian objects and is comparable in size to the largest main-belt asteroid, 1 Ceres. Farnham (2001) reported a rotational lightcurve from observations taken 2001 Jan 24 – 27 with a single-peaked period 3.17 hr and ”amplitude” 0.5 mag. Farnham also found other plausible periods including 2.78 and 3.67 hrs. Motivated by this remarkable result, we immediately undertook observations to secure an independent determination of

the lightcurve, and to search for rotational color variations. Such variations are predicted by the impact resurfacing model (Luu and Jewitt 1996). In this paper we will discuss Varuna’s lightcurve, possible causes of the brightness variations, and what this object may reveal about the collisional environment in the young Trans-Neptunian belt.

2. Observations

Optical observations were taken UT 2001 February 17 - 21 and April 22, 24 and 25 at the University of Hawaii 2.2-m telescope atop Mauna Kea, Hawaii. We used a Tektronix 2048×2048 pixel charge-coupled device (CCD), having 0.219 arcsec per pixel image scale and a 7 arcminute field of view. Images were secured through standard broadband BVRI filters based on the Johnson Kron-Cousins system. The CCD bias level was determined from an overclocked region of the chip. Flat field calibration was obtained using a mixture of images of the twilight sky with data frames. The image quality (including contributions from the telescope, wind shake and atmosphere) varied from 0.6 to 1.2 arcsec Full Width at Half Maximum (FWHM), but was mostly concentrated near a mean at 0.7 arcsec. Absolute calibration of the data was obtained through repeated observations of standard stars from the list by Landolt (1992). The position of Varuna was dithered over the detector to prevent pathological problems in the photometry associated with bad pixels. Images photometrically affected by proximity to bad pixels or field stars and galaxies (including all those from UT 2001 February 21), were rejected from further analysis.

For the purposes of lightcurve determination, Varuna was compared to a network of field reference stars in each image. The field stars were selected to be near Varuna in the sky and to have Sun-like or slightly redder colors. Where possible, we employed the same field reference stars each night to minimize systematic photometric errors. This procedure effectively removes the influence of atmospheric extinction (which, at the high altitude

of Mauna Kea, is already small, amounting to only about 0.08 mag. per airmass in the R-band). The latter part of the night of UT 2001 February 19 was slightly non-photometric (deviations were \sim few 0.01 mag.) but, otherwise, we benefited from clear skies. Effects of seeing variations between images were minimized by using multi-aperture photometry. Small apertures (typical radii \sim 1 arcsec) were used to relate Varuna to the field star network in each field. Large apertures (typical radii \sim 3.0 arcsec) were used to relate the field stars to the Landolt standards. The median sky level was determined within a contiguous annulus having outer radius 5 arcsec. At the time of the observations, Varuna moved westward at about 2 arcseconds per hour. The image trailing due to the motion of Varuna was only \sim 0.1 arcseconds during a typical 200 second integration. This is small compared to our nominal 0.7 arcsecond FWHM image quality and, therefore, trailing losses are an unimportant source of error in our photometry.

A journal of observations including the geometric circumstances is given in Table 1. The R-band photometry is listed in Table 2. Periodicity in the photometry was obvious even in preliminary reductions of the first night’s data conducted at the telescope, as may be seen in Figure 1.

3. Results

The apparent magnitude varied in the approximate range 19.50 to 19.95, with a mean near 19.7. Periodicity in the R-band photometry was sought using a) the PDM (phase dispersion minimization) method (Stellingwerf 1978) and b) the related but different SLM (string length minimization) method (Dworetzky 1983). The PDM and SLM results were in all cases consistent; for brevity we here present only the results from PDM. Figure 2 shows the PDM theta parameter as a function of rotational frequency for the entire R-band photometry data set (the closer theta is to zero, the better the fit: see Stellingwerf (1978) for

more information). Broad, deep minima occur near the lightcurve frequencies $P^{-1} = 7.57$ day $^{-1}$ and $P^{-1} = 3.78$ day $^{-1}$. The first corresponds to a single-peaked lightcurve with a period near $P = 3.17$ hr, close to the 3.17 hr period reported by Farnham (2001). The second minimum corresponds to the double-peaked lightcurve of 6.34 hr. The minima are flanked by aliases due to the 24-hour sampling periodicity that is imposed on the data by the day-night cycle (see the theta minima in Figure 2 displaced from the primary by $\pm n$ day $^{-1}$, where $n = 1, 2, 3 \dots$). The phased lightcurves produced using the 24-hr alias periods of the single-peaked lightcurve ($P^{-1} = 6.5$ day $^{-1}$, 8.6 day $^{-1}$) are unconvincing. When viewed at high resolution, the primary minimum of the theta plot for the single-peaked lightcurve is seen to be split by a finely spaced series of minima due to the ~ 65 day data gap between the February 2001 and April 2001 observations (Figure 3). The lightcurves produced by phasing the data at each of the lowest 3 minima in Figure 3 (3.1656, 3.1721, and 3.1788 hours) appear comparably good to the eye. In this sense, the rotation period cannot be exactly determined from the present data, although we are confident that, if Varuna’s lightcurve is single-peaked, the true period is given by one of the 3 minima in Figure 3. Subject to this caveat, we adopt $P = 3.1721 \pm 0.0001$ hrs as the best fit to the single-peaked lightcurve period.

Is the lightcurve single or double-peaked? Close inspection of the raw and phased data suggests that the lightcurve of Varuna has two maxima per rotation period. This is evident in Figure 4, where phased lightcurves show that the first and second lightcurve minima have slightly different shapes. Therefore, we adopt the double-peaked lightcurve ($P_{rot} = 6.3442 \pm 0.0002$ hrs) as the probable rotation period of Varuna (subject to the caveat that very nearby alias periods 6.3317 and 6.3574 hours are also plausible fits to the data as discussed for the single peaked aliases above). Our best estimate for the photometric range of the data is $\Delta m = 0.42 \pm 0.02$ mag.

We used the preliminary photometry to target color measurements near the extrema of the R-band brightness, in order to search for rotational color variations. Color measurements in B, V and I filters were interleaved with R-band photometry so as to correct for photometric trends caused by the rotation. The color measurements are summarized in Table 3 and plotted versus rotation phase in Figure 5. There it may be seen that our data provide no evidence for rotational modulation of the color of the scattered radiation. Specifically, the B-V, V-R and R-I color indices are constant with rotational phase at the level of accuracy of the measurements, as seen in Table 3. The mean colors found for Varuna, $B - V = 0.85 \pm 0.02$, $V - R = 0.64 \pm 0.01$, $R - I = 0.62 \pm 0.01$ and $B - I = 2.11 \pm 0.02$ (Table 3) are compatible with the mean colors of 12 other classical TNOs measured independently (Jewitt and Luu 2001: $B - V = 1.00 \pm 0.04$, $V - R = 0.61 \pm 0.03$, $R - I = 0.60 \pm 0.04$ and $B - I = 2.22 \pm 0.10$). Although larger than most, Varuna is not colorimetrically distinguished from the other TNOs.

4. Interpretation

The rotational lightcurve of a Solar System body results from the combined effects of aspherical body shape and azimuthal albedo variations. Double-peaked lightcurves are the expected signature of a prolate body in rotation about its minor axis. However, this interpretation is not unique: an appropriate arrangement of albedo markings can reproduce any lightcurve (Russell 1906). The large size of Varuna suggests that any elongation of the body is probably caused by a large specific angular momentum and the resulting rotational deformation. Here, we consider the two limiting cases in which a) the lightcurve is produced entirely by albedo variations across the surface of Varuna and b) the lightcurve is produced by rotational modulation of the geometric cross section of Varuna due to aspherical shape. The real situation of Varuna will naturally lie somewhere between these two extremes.

4.1. Albedo Models

A complex distribution of albedo markings could produce the observed lightcurve. If so, the $\Delta m_R = 0.42 \pm 0.02$ magnitude photometric range would imply an albedo contrast $10^{0.4\Delta m_R} \approx 3 : 2$ or greater (depending on the projection of the rotation vector into the line of sight). Some spherical outer Solar System bodies show large albedo contrasts, notably Iapetus (Millis 1977) and Pluto (Buie, Tholen and Wasserman 1997). On Iapetus, the albedo contrast is associated with a color variation, the dark material being redder than the bright material (Table 4). Rotational color variations on Varuna as large as those on Iapetus would be apparent in our data if they were present. Pluto’s hemispherical albedo contrast is matched by a corresponding color variation that is barely measurable even in this bright object (Table 4). Large color differences exist between local surface units on Pluto ($0.77 \leq B - V \leq 0.98$; Young, Binzel and Crane 2001) but hemispherically averaged color variations occur only at the 0.01 mag. level and are so small that they would not be detected in the present work (Table 4). From the example set by Pluto, we conclude that the absence of color variations on Varuna larger than a few $\times 0.01$ mag. places no useful constraint on the albedo modulation hypothesis.

If Varuna is spherical and rotating at period P , we can obtain a lower limit to the density by requiring that the body not be in a state of internal tension. Simple force balance then gives

$$\rho = \frac{3\pi}{GP^2} \tag{1}$$

where $G = 6.67 \times 10^{-11}$ [N kg⁻² m²] is the gravitational constant and $P[s]$ is the rotation period. With $P = 3.17$ hr, Eq. (1) gives a lower limit to the density as $\rho = 1090$ kg m⁻³. The hydrostatic pressure at the center of a 450 km radius object with this density

is $\sim 6 \times 10^7 \text{ N m}^{-2}$. A body as large as Varuna will almost certainly not possess the strength needed to maintain spherical shape when rotating with a 3 hr period (note that the rotations of the comparison objects Iapetus and Pluto are tidally locked, with periods 79 and 6.4 *days*, respectively, so that rotational deformation is small). Therefore, we believe that the spherical albedo model of Varuna is physically implausible. Instead, we next discuss models in which the shape, not the albedo, is primarily responsible for the observed lightcurve variations.

4.2. Shape Models

A more likely model is one in which Varuna is rotationally deformed by the centripetal forces associated with its rapid rotation. As in the asteroid belt, large impacts that do not completely destroy a body may disrupt it into a self-gravitationally bound, strengthless "rubble pile" (Farinella et al. 1981). Rubble-pile bodies will re-assemble after impact into a shape determined by their angular momentum, H , and density, ρ . Following the convention of Chandrasekhar (1987), we write the angular momentum in units of $(GM^3a')^{1/2}$, where M [kg] is the body mass and a' [m] is the radius of the equal-volume sphere. At $H = 0$, the equilibrium shape is the sphere. As H increases, a perfectly strengthless fluid deforms first into an oblate (so-called MacLaurin) spheroid in rotation about its minor axis (Chandrasekhar 1987). The MacLaurin spheroids become progressively more flattened up to the critical value $H = 0.304$, above which the body becomes triaxial (a Jacobi spheroid). At $H \geq 0.390$, the Jacobi spheroids are rotationally unstable and the object splits into a binary. This rotational deformation sequence is highly idealized when applied to solid bodies, of course, because even a rubble pile will not respond to rotational stresses in the same way as a perfectly strengthless fluid. A fractured body will have a "grainy" structure, perhaps with large, coherent internal blocks that will retain expression in the

final body shape. Nevertheless, the MacLaurin-Jacobi spheroids represent a limiting case with which the asteroids and TNOs may usefully be compared. Evidence for the existence of rubble-piles among the main-belt asteroids is limited and indirect but nevertheless suggestive. For example, small asteroids ($D \leq 100$ km) have a distribution of body shapes that is consistent with those of fragments from hypervelocity impact experiments in the laboratory (Catullo et al. 1984). On the other hand, larger asteroids are deficient in highly elongated bodies relative to the fragment shape distribution, perhaps because their shapes have relaxed towards rotational equilibrium (Farinella et al. 1981). As we note below, a few well-measured asteroids have densities less than the density of solid rock, suggesting a porous internal structure that could be produced by re-accumulation of large blocks in a rubble-pile (Yeomans et al. 1999). TNOs larger than about 100 km in diameter are massive enough to survive collisional disruption over the age of the solar system but may nevertheless have been internally fractured into rubble piles (Farinella and Davis 1996).

Since an oblate spheroid in principal axis rotation about its axis of maximum moment of inertia offers no rotational modulation of the cross-section, we conclude that the MacLaurin spheroids cannot explain the lightcurve of Varuna, and that $H > 0.304$ for this object. However, the triaxial Jacobi spheroids with $0.304 \leq H \leq 0.390$ present plausible solutions for the shape of Varuna. For the Jacobi spheroids, knowledge of the rotation period and the shape (from Δm) provide a unique measure of the density. With $P = 6.34$ hr and axis ratio $10^{0.4\Delta m} \approx 3 : 2$, we obtain $\rho = 1050 \text{ kg m}^{-3}$ from the tables of Chandrasekhar (1987). Since the axis ratio can only be a lower limit (because of projection), the derived density is also a lower limit. This value is close to the density estimated from the spherical albedo model, above, but has the advantage that it is derived from a physically more plausible model. A Jacobi ellipsoid's three axes ($a > b > c$) depend strongly on each other. By using the axis ratio for a and b above we find the ratio for all three as 3:2:1.4 (Chandrasekhar 1987). Here 1.4 refers to the rotation axis (c) which can not be observed directly through the lightcurve

if the object is in principal axis rotation.

4.3. Binary

We also consider the possibility that Varuna is a binary, in which case the lightcurve would result from occultation of one component by the other. The short period and lightcurve shape of Varuna require that the binary components must be close or even in contact, leading to mutual gravitational deformation of the components. We will consider these effects momentarily. However, it is physically illuminating to first discuss the limiting case in which the binary components are in contact but retain a spherical shape. Suppose that the primary and secondary components have radii a_p and a_s , respectively. The barycenter of the contact binary will be separated from the center of the secondary by a distance

$$l = (a_p + a_s) \left(\frac{m_p}{m_p + m_s} \right) \quad (2)$$

where m_p and m_s are the masses of the primary and secondary, respectively. Force balance then gives a relation between the angular frequency, density and mass ratio, namely $l\omega^2 = Gm_p/(a_p + a_s)^2$. Assuming that both components have density ρ [kg m^{-3}], we obtain

$$\rho = \frac{3\pi}{GP^2} \left[\frac{(1 + (a_s/a_p))^3}{1 + (a_s/a_p)^3} \right] \quad (3)$$

The ratio a_s/a_p can be estimated from the photometric range of the lightcurve. Specifically, the range in magnitudes is given by

$$\Delta m = 2.5 \log \left[\frac{a_s^2 + a_p^2}{a_p^2} \right] \quad (4)$$

which can be rearranged to yield

$$\frac{a_s}{a_p} = (10^{0.4\Delta m} - 1)^{1/2} \quad (5)$$

From Equation 5, the Varuna lightcurve range ($\Delta m = 0.42$ mag.) suggests an axis ratio $a_s/a_p = 0.69$, corresponding to mass ratio $m_s/m_p = (a_s/a_p)^3 = 0.32$. Equations 3 and 5 together give the density in terms of the two observable quantities P and Δm :

$$\rho = \frac{3\pi}{GP^2} \left[\frac{(1 + (10^{0.4\Delta m} - 1)^{1/2})^3}{1 + (10^{0.4\Delta m} - 1)^{3/2}} \right]. \quad (6)$$

Substitution of $P = 6.3$ hrs, $\Delta m = 0.42$ mag. into Equation 6 gives $\rho = 996$ kg m⁻³. This is a lower limit to the density since, due to projection effects, the observations provide only a lower limit to Δm . However, given the crudeness of this model, it is interesting that we obtain essentially the same density as from the Jacobi spheroid approximation. We conclude that binary models with the observed period and physically plausible densities can account for the Varuna lightcurve. There remains, however, no specific evidence that Varuna is a binary object.

Lastly, Leone et al. (1984) present calculations that partially account for the mutual deformation of the components in a close binary. The solutions are non-unique, since different combinations of m_s/m_p and density lead to the same P , Δm pair. Here, we simply refer to their Table 1, and note a plausible solution near $\rho \approx 3600$ kg m⁻³ and $m_s/m_p \approx 0.2$. This bulk density is much higher than is required than in our simple, spherical contact binary model since the components are more widely separated (the Roche radius is \sim twice the component radius) and therefore orbit more slowly for a given mass. For several reasons we believe the Roche model and the Leone et al. calculations are not well-suited to the case of Varuna. In particular, the wide separation reduces the probability that the system would

be aligned so as to produce mutual eclipses. Furthermore, the nearly sinusoidal lightcurve shape is not easily produced by a wide pair in which we would expect the eclipses and occultations to occupy a smaller fraction of rotational phase space. Varuna’s lightcurve does not show the notched appearance characteristic of eclipsing binary stars.

5. Discussion

5.1. The Density of Varuna

The bulk density derived in Section 4 is only slightly higher than the density of water ice. Strictly speaking, the derived density is a lower limit because of the effects of projection into the plane of the sky. However, it is unlikely that the density is much (factor of two) higher than 1000 kg m^{-3} if our equilibrium rotator model is correct. The simplest interpretation, namely that the rock content of Varuna is small or negligible, is difficult to accept on physical grounds: accretion of planetary solids in a dusty circumsolar disk provides no obvious fractionation mechanism to lead to the formation of a pure ice ball. Here, we explore the possibility that Varuna’s low density is caused by an internal structure that is at least partly porous.

We represent Varuna as a composite of volatile matter (ice), refractory matter (rock) and void space. The mean density of this composite is

$$\bar{\rho} = \rho_i f_i + \rho_r f_r \tag{7}$$

where ρ_i and ρ_r are the densities of ice and rock, and f_i and f_r are the fractional volumes occupied by ice and rock, respectively. We require

$$f_i + f_r + f_v \equiv 1, \quad (8)$$

where f_v is the fractional void space, also known as porosity. The fraction of the total mass carried by refractories is

$$\psi = \frac{\rho_r f_r}{\rho_r f_r + \rho_i f_i}. \quad (9)$$

Equations (7) - (9) combine to give

$$f_v = 1 - \frac{\bar{\rho}}{\rho_i} \left[1 + \psi \left(\frac{\rho_i}{\rho_r} - 1 \right) \right]. \quad (10)$$

The hydrostatic pressure at the core of Varuna is about $6 \times 10^7 \text{ N m}^{-2}$, while the mass-weighted internal temperatures are likely to average $\sim 100 \text{ K}$ ($\sim 50 \text{ K}$ at the surface, slowly rising towards the core as a result of internal radioactive decay heating). Under these conditions the ice-I polymorph of water, for which $\rho_i = 940 \text{ kg m}^{-3}$ (Lupo and Lewis 1979), is the stable phase. The density of the refractory matter, ρ_r , is less certain and we compute models using two representative values. First, we take $\rho_r = 3000 \text{ kg m}^{-3}$ as representative of the densities of a number of plausible silicates, notably Forsterite (Mg_2SiO_4) which has been spectroscopically detected in comets. Second, we take $\rho_r = 2000 \text{ kg m}^{-3}$ to represent the less dense CHON type hydrocarbon materials that are also found in comets.

The resulting values of the porosity are plotted against the rock fraction in Figure 6, where we have adopted $\bar{\rho} = 1000 \text{ kg m}^{-3}$ (solid lines) from the lightcurve models. To show the sensitivity to the mean density we also plot in Figure 6 the porosities derived if $\bar{\rho} = 1200 \text{ kg m}^{-3}$ (dashed lines).

Figure 6 shows that non-porous ($f_v = 0$) models restrict the rock fraction to $\psi \sim 0.1$

($\bar{\rho} = 1000 \text{ kg m}^{-3}$) to $\psi \sim 0.35$ ($\bar{\rho} = 1200 \text{ kg m}^{-3}$). Larger rock fractions require non-zero porosity; cosmochemically plausible $\psi = 0.5$ implies $0.05 \leq f_v \leq 0.30$ for the parameters considered here. The few measured nuclei of comets have densities in the range $500 - 1000 \text{ kg m}^{-3}$ (Sagdeev et al. 1988, Rickman 1989, Asphaug and Benz 1996) and rock fractions $\psi \geq 0.5$ (corresponding to rock/ice mass ratios ≥ 1 , Lisse et al. 1998, Jewitt and Matthews 1999). Given that the Jupiter family comets are collisionally produced fragments of the trans-Neptunian objects (Farinella and Davis 1996), large ψ may well be representative of Varuna and related objects.

Are porosities up to several 10's of % physically plausible in a body of Varuna's size? We argue first by analogy. Materials on planetary surfaces are commonly porous. Carbonate ($CaCO_3$) Waikiki beach sand, for instance, has porosity $f_v \sim 0.4$ while the basaltic lunar regolith has $0.4 \leq f_v \leq 0.7$ (Carrier et al. 1974). The mechanical compression of carbonate and quartz sands (SiO_2) has been studied experimentally to pressures rivalling that in Varuna's core (Chuhan et al. 2002). Sand samples having porosity $f_v = 0.4$ to 0.5 at atmospheric pressure compress only to $f_v \sim 0.2$ to 0.3 at $5 \times 10^7 \text{ N m}^{-2}$. At pressures $\leq (2 \text{ to } 6) \times 10^6 \text{ N m}^{-2}$ the densification occurs by rearrangement of the irregular silicate grains while, at higher pressures, the densification occurs by grain crushing and the filling-in of void space. Crushing is particularly important in large-grain sands where the number of grain-grain contacts is small and the contact pressures are high. In any event, this direct experimental evidence shows that aggregates of silicate (and carbonate) grains can remain substantially porous throughout the range of pressures prevailing inside Varuna. The physical reason is the large compressive strength of the grain materials.

When at low temperatures, water ice also possesses a large compressive strength ($1.2 \times 10^8 \text{ N m}^{-2}$ at 158 K rising to $1.7 \times 10^8 \text{ N m}^{-2}$ at 77 K ; Durham et al. 1983) giving a response to hydrostatic loading qualitatively similar to that of sand. However,

the experimental situation for ice grain aggregates is less clear, mainly because most experiments have been performed at temperatures and strain-rates higher than are relevant to outer solar system bodies. The most relevant experiments of which we are aware were conducted at 213 K over the 0.8 to 8.2×10^8 N m⁻² pressure range (Leliwa-Kopystynski et al. 1994). They show that substantial porosity can exist in ice/rock grain mixtures at all pressure levels found inside Varuna. We conclude that porosity is a potentially important factor in determining the bulk constitutions of the TNOs.

Several of the outer planet satellites are similar to Varuna in both size and density. For example, Saturnian satellite SIII Tethys has density $\bar{\rho} = 1210 \pm 160$ kg m⁻³ and is 524 ± 5 km in radius (Smith et al. 1982). The Uranian satellite UII Umbriel has density 1440 ± 280 kg m⁻³ and radius 595 ± 10 km (Smith et al. 1986). Even the much larger and, presumably, self-compressed object Iapetus (radius 730 ± 10 km) has a low density of only 1160 ± 90 kg m⁻³ (Smith et al. 1982). Internal porosity (due to the granular structure of the constituent materials) may account for the low densities of these satellites while simultaneously allowing rock fractions $0.28 \leq \psi \leq 0.66$ (Kossacki and Leliwa-Kopystynski 1993). Within the uncertainties, these bodies all have densities consistent with that derived here for Varuna. Unlike Varuna, they are nearly spherical in shape, but this is because the satellites are tidally locked with rotation periods measured in days, not hours, and the centripetal accelerations are consequently very small. If rotating with Varuna’s angular momentum, they would adopt prolate body shapes and display large rotational lightcurves.

The larger object Pluto has $\rho \approx 2000$ kg m⁻³ (Tholen and Buie 1997): the corresponding rock-fraction from Eq. (10) (assuming $f_v = 0$ and considering higher pressure ice phases) is $\psi \sim 0.7$. Core hydrostatic pressure (which scales as $\rho^2 r^2$) is larger in Pluto than in Varuna by a factor ~ 25 . For this reason it is natural to expect that the influence of porosity on the bulk density should be greatly reduced relative to the Varuna case.

A different source of porosity is suggested by the 50 km diameter and (presumably) rocky main-belt asteroid 253 Mathilde, which is of surprisingly low density (1300 ± 200 kg m⁻³; Yeomans et al. 1999). This may reflect macroscopic porosity ($\sim 50\%$) resulting from the loose re-accumulation of a fractured body into a rubble-pile structure. In Varuna, microscopic and macroscopic porosity may co-exist, the former from the slow accretion of grains at low temperatures and the latter from an energetic, terminal collision phase.

Varuna is one of the largest known trans-Neptunians, with a diameter $D = 900(+125/ - 145)$ km (1σ error bars; Jewitt, Aussel and Evans 2001). Even the 3σ lower limit to the diameter, 465 km, leaves this as an object of imposing dimensions. But Varuna is not entirely alone in its combination of large size, short period and aspherical shape: there are a few large asteroids which have both large photometric ranges and short periods. Notable examples include 15 Eunomia (diameter 256 km, period 6.08 hr, photometric range 0.56 mag.), 87 Sylvia (270 km, 5.18 hr, 0.62 mag.) and 107 Camilla (222 km, 4.84 hr, 0.52 mag.). Like Varuna, these may be bodies of low strength which are rotationally deformed due to a large amount of angular momentum delivered by collisions (Farinella et al. 1981). Collectively, these observations show that the low density of Varuna, as deduced from its lightcurve, is unremarkable when viewed in the context of other solar system objects.

5.2. High Specific Angular Momentum in the Trans-Neptunian Belt

The discussion in Section 4 shows that Varuna must possess a high specific angular momentum, $0.304 \leq H \leq 0.390$, close to the value needed to cause rotational breakup. This immediately suggests a parallel with the 4 known Trans-Neptunian binaries, Pluto-Charon (Tholen and Buie 1997), 1998 WW31 (Veillet 2001), 2001 QT297 (Elliot et al. 2001) and 2001 QW322 (Kavelaars et al. 2001) because these systems also possess high specific

angular momenta. Of these four, Pluto-Charon is by far the best characterised (neither the sizes/masses nor the eccentricities of the other binary systems are yet known, preventing the determination of their specific angular momenta at a diagnostically useful level). In the Pluto-Charon system the angular momentum is primarily contained within the orbital motion of the components (i.e., the spin angular momentum is small). If the mass and angular momentum of Pluto and Charon were to be combined into a single body, that object would have $H \approx 0.45$ (McKinnon 1989) and would be unstable to rotational breakup. This fact suggests that Pluto and Charon were formed by a glancing impact between precursor objects (McKinnon 1989, Dobrovolskis et al. 1997). It is not yet clear that the other (much less massive) TNO binaries formed in a similar way, but their high specific angular momenta nevertheless suggest that collisions played an important role. We believe that Varuna is an intermediate case in which a collision between massive precursors produced a spin rapid enough to cause global deformation but not sufficient to cause rotational breakup.

The current collision rate amongst Trans-Neptunian Objects is too low to substantially modify the spins of objects as large as Pluto and Varuna. Instead, their H must have been acquired through late-stage collisions at the end of the ~ 100 Myr (Kenyon and Luu 1999) formation period. We use this to constrain the collisional environment in the young Trans-Neptunian belt. Since the applicable parameters are not well known, an order of magnitude (particle-in-a-box) type calculation is appropriate. Our objective is to estimate the density of objects in the Trans-Neptunian belt needed to produce collisional breakup of a measurable fraction of the Varuna-sized objects within the 100 Myr formation period. Collisional breakup does not guarantee the formation of a binary, and may not lead to a high specific angular momentum in the target object, but it is a necessary step towards these ends.

We first represent the TNO size distribution by a power law, in which the number of

objects per unit volume with radii in the range a to $a + da$ is $n(a)da = \Gamma a^{-q} da$, where Γ and q are constants. The timescale for the collisional disruption of a non-rotating, spherical target TNO of radius a_T is given by

$$\tau^{-1} = \int_{a_C}^{\infty} 4\pi (a_T + a)^2 \Gamma a^{-q} \Delta V da. \quad (11)$$

Here, a_C is the critical radius of the smallest projectile capable of producing disruption and ΔV is the impact velocity. The constant Γ is obtained from the data by normalizing to the Trans-Neptunian belt population, such that

$$\int_{a_{50}}^{\infty} \Gamma a^{-q} da = \frac{N_{50}}{W} \quad (12)$$

where N_{50} is the number of TNOs larger than $a_{50} = 50$ km in radius, and W is the effective volume swept by the classical TNOs. We take $q = 4$, $\Delta V = 1.3$ km s^{-1} , $N_{50} = 4 \times 10^4$ (Trujillo, Jewitt and Luu 2001) and represent the classical belt as an annulus with inner and outer radii of 40 AU and 50 AU, respectively, and thickness 10 AU, giving $W \approx 9.5 \times 10^{38}$ m^3 . Hence, $\Gamma = 1.6 \times 10^{-20}$ by Eq. (12).

For spherical target and projectile TNOs of equal density, the critical projectile radius for disruption is given by

$$\frac{a_C}{a_T} = \left(\frac{2\epsilon}{\Delta V^2} \right)^{1/3}. \quad (13)$$

where $\epsilon \approx 10^5$ J kg^{-1} is the specific energy for disruption (Love and Ahrens 1996).

Combining these relations and substituting, we obtain

$$\tau \approx 2.5Gyr \left[\frac{a_T}{1km} \right] \left[\frac{4 \times 10^4}{N_{50}} \right] \quad (14)$$

as our estimate of the collisional lifetime of a TNO of radius a_T in the present day, low-density Trans-Neptunian belt. Varuna-scale objects ($a_T \sim 450$ km) have lifetimes to collisional disruption $\tau \sim 1 \times 10^{12}$ yr (Eq. 14), much longer than the 4.6×10^9 yr age of the solar system (Farinella and Davis 1996). Under these circumstances, large collisionally produced binaries and objects of high specific angular momentum should not be common.

The frequencies of occurrence of rotationally distorted and binary TNOs both remain to be determined with accuracy. Objects 1998 SM165 and 2000 GN171 have independently been reported to show large rotational variations (Romanishin et. al 2001, Sheppard 2001) and, from the available data, it appears likely that large amplitude objects like Varuna are common, as are binary TNOs. We conservatively estimate that a fraction $f \geq 1\%$ of the TNOs are binaries and/or rotationally distorted objects of high intrinsic angular momentum. If the formation phase took $\tau_f \sim 10^8$ yr (Kenyon and Luu 1999), then the corresponding disruption timescale is of order $f^{-1}\tau_f \leq 10^{10}$ yrs. With this timescale and $a_T = 450$ km (for Varuna), Eq. (14) gives $N_{50} \sim 5 \times 10^6$, about 100 times the current number of large TNOs. The current mass of the TNOs is about 0.1 to 0.2 M_\oplus (Jewitt, Luu and Trujillo 1998, Trujillo, Jewitt and Luu 2000). Thus, from the high incidence of binaries and rotationally distorted objects, we infer an initial mass $M_i \geq 10$ to 20 M_\oplus in the Classical region of the Trans-Neptunian belt. Numerical accretion calculations give the time for Trans-Neptunian objects to grow to 1000 km scale as $\tau \sim 280$ Myr ($10 M_E / M_i$) (Kenyon and Luu 1999). Substituting for M_i we obtain $\tau \sim 140$ to 280 Myr, comparable to the ~ 100 Myr timescale estimated for the formation of Neptune.

Efficient growth of the TNOs required a small velocity dispersion. Growth models show that mutual scattering by ever larger bodies produced an increase in the velocity

dispersion, ultimately resulting in collisional shattering of the smaller objects (Kenyon and Luu 1999). The broad inclination and eccentricity distributions of the current TNOs suggest that another process, perhaps the appearance of nearby Neptune or, conceivably, an external perturber (Ida et al. 2000), increased the velocity dispersion to values even higher than could be attained through mutual scattering. The collisional events leading to Varuna’s rapid rotation and the break-up of TNOs probably occurred in this final stage.

On-going measurements of the lightcurves, spin states and binarity of a statistical sample of TNOs will show the extent to which the shapes of these bodies are determined by their angular momenta (see Sheppard and Jewitt 2002). Detection of a large proportion of high H objects would strengthen our conclusion that the past environment in the Trans-Neptunian belt was one in which collisions between massive bodies were common. The role of porosity will be illuminated by future measurements of TNO densities, perhaps based on careful astrometric and physical studies of the growing sample of binary objects. We expect a trend towards higher densities at larger diameters, at least amongst those TNOs that have survived intact (although fractured) since the formation of the solar system. Smaller objects, particularly the 1 to 10 km scale bodies sampled locally in the Jupiter-family comets may display a wide range of densities influenced both by the density (hence, size) of the target from which they were eroded and by densification during the collisional process.

6. Summary

1) High precision, time series photometry of trans-Neptunian object (20000) Varuna reveals a sustained, periodic modulation of the apparent brightness. In data from 2001 February and April, the best-fit rotation period is double-peaked with a 6.3442 ± 0.0002 hour period. The photometric range is $\Delta m = 0.42 \pm 0.02$ mag. The B-V, V-R and R-I

colors are completely typical of TNOs and show no variation with rotational phase, down to the level of a few per cent.

2) We interpret Varuna as a centripetally distorted, prolate ellipsoid, with an axis ratio $\geq 3:2$ and density $\rho \approx 1000 \text{ kg m}^{-3}$. The specific angular momentum, $0.304 \leq H \leq 0.390$, is high (objects with $H > 0.390$ are rotationally unstable and break up).

3) The low bulk density of Varuna requires significant porosity (up to several 10's of %) if the rock mass fraction is cosmochemically typical (~ 0.5). In this respect, Varuna is similar to the icy satellites of Saturn and Uranus, many of which show bulk densities near that of water ice. Porosity could occur on a microscopic level due to granular structure of the constituent material, or macroscopically if Varuna has been loosely re-assembled after fracturing by past impacts.

4) The high specific angular momentum of Varuna cannot have been supplied by collisions in the present-day, low-density Trans-Neptunian belt. High H leading to rotational deformation and binary formation suggests an early, high density phase in the Trans-Neptunian belt. We infer an initial mass $M_i \sim 10$ to $20 M_{\oplus}$ from the apparently high incidence of binaries and rapidly rotating Trans-Neptunian Objects.

Acknowledgments

We thank John Dvorak and Paul deGroot for operating the UH telescope, Jane Luu, Yan Fernandez and the anonymous referee for comments on the manuscript and Fawad Chuhan for pointers about the literature of sand. This work was supported by a grant to DCJ from the National Science Foundation.

REFERENCES

- Asphaug, E. and Benz, W. (1996). *Icarus*, 121, 225-248.
- Bowell, E., Hapke, B., Domingue, D., Lumme, K., Peltoniemi, J., and Harris, A. (1989) Asteroids II, edited by R. Binzel, T. Gehrels and M. Matthews, Univ. Az. Press, Tucson, pp. 524-556.
- Buie, M., Tholen, D., and Wasserman, L. (1997). *Icarus*, 125, 233.
- Capaccioni, F., Cerroni, P., Coradini, M., Farinella, P., Flamini, E., Martelli, G., Paolicchi, P., Smith, P. N., and Zappala, V. (1984). *Nature*, 308, 832-834.
- Carrier, W., Mitchell, J., and Mahmood, A. (1974). *Proc. Fifth Lunar Sci. Conf., Suppl. 5.*, *Geochim. Cosmochim. Acta*, 3, 2361-2364.
- Catullo, V., Zappala, V., Farinella, P., and Paolicchi, P. (1984). *Astron. Ap.*, 138, 464-468.
- Chandrasekhar, S. (1987). *Ellipsoidal Figures of Equilibrium*. Dover, New York.
- Chuhan, F., Kjeldstad, A., and BJORLYKKE, K. (2002). *Marine and Petroleum Geology*, in press.
- Dobrovolskis, A., Peale, S., and Harris, A. (1997). In *Pluto and Chiron*, eds. A. Stern and D. Tholen, Univ. Az. Press, Tucson, pp. 159.
- Durham, W., Heard, H., and Kirby, S. (1983). *Journal Geophys. Res.*, 88, B377-B392.
- Dworetzky, M. M. (1983). *MNRAS*, 203, 917-924.
- Elliot, J., Kern, S., Osip, D., and Burles, S. (2001). *IAU Circular 7733* (October 15).
- Farnham, T. (2001). *IAU Circular 7583* (February 16)
- Farinella, P., Paolicchi, P., Tedesco, E., and Zappala, V. (1981). *Icarus*, 46, 114-123.
- Farinella, P.; Davis, D. R. (1996). *Science*, 273, 938-941
- Ida, S., Larwood, J., and Burkert, A. (2000). *Ap. J.*, 528, 351-356.

- Jewitt, D., Luu, J., and Trujillo, C. (1998). *Astron. J.*, 115, 2125.
- Jewitt, D. and Matthews, H. (1999). *Astron. J.*, 117, 1056-1062.
- Jewitt, D. and Luu, J. The Kuiper Belt. In *Protostars and Planets IV*. Edited by Vince Mannings, A. Boss and S. Russell, University of Arizona Press, Tucson. pp:1201-1229. (2000).
- Jewitt, D., Aussen, H., and Evans, A. (2001). *Nature*, 411, 446-447.
- Jewitt, D. and Luu, J. (2001). *Astron. J.*, 122, 2099-2114.
- Kavelaars, J., Petit, J., Gladman, B., and Holman, M. IAU Circular 7749 (November 9).
- Kenyon, S. and Luu, J. (1999). *Astron. J.*, 118, 1101- 1119.
- Knofel, A. and Stoss, R. (2000). *Minor Planet Electronic Circular No. 2000- Y45* (Dec 31).
- Kossacki, K., and Leliwa-Kopystynski, J. (1993). *Planet. Space Sci.*, 41, 729-741.
- Landolt, A. (1992). *Astron. J.*, 104, 340 - 371.
- Leliwa-Kopystynski, J., Makkonen, L., Erikoinen, O., and Kossacki, K. (1994). *Planet. Space Sci.*, 42, 545-555.
- Leone, G., Farinella, P., Paolicchi, P., and Zappala, V. (1984). *Astron. Ap.*, 140, 265-272.
- Lisse, C., A'Hearn, M., Hauser, M., Kelsall, T., Lien, D., Moseley, S., Reach, W. and Silverberg, R. (1998). *Ap. J.*, 496, 971-991.
- Love, S., and Ahrens, T. (1996). *Icarus*, 124, 141-155.
- Lupo, M. and Lewis, J. (1979). *Icarus*, 40, 156
- Luu, J., and Jewitt, D. (1996). *Astron. J.*, 112, 2310
- McKinnon, W. (1989). *Ap. J.*, 344, L41-L44.
- McMillan, R., and Larsen, J. (2000). *Minor Planet Electronic Circular 2000-X02* (Dec. 01)
- Millis, R. (1977). *Icarus*, 31, 81-88.

- Rickman, H. (1989). *Advances in Space Research*, 9, 59-71.
- Romanishin, W., Tegler, S., Rettig, T., Consolmagno, G., and Botthof, B. (2001). *Proc. Nat. Academy Sci.*, 98, 11863.
- Russell, H. (1906). *Ap. J.*, 24, 1-18.
- Sagdeev, R. Z.; Elyasberg, P. E.; Moroz, V. I. (1988). *Nature*, 331, 240-242.
- Sheppard, S. and Jewitt, D. (2002). Submitted
- Sheppard, S. (2001). *IAU Circular* 7619 (May 4).
- Smith, B. A. et al. (1982). *Science*, 215, 504-537.
- Smith, B. A. et al. (1986). *Science*, 233, 43-64.
- Stellingwerf, R. F. (1978). *Ap. J.*, 224, 953-960.
- Tholen, D., and Buie, M. (1997). In *Pluto and Charon*, eds. S. A. Stern and D. J. Tholen, Univ. Az. Press, Tucson, pp. 193-220.
- Trujillo, C., Jewitt, D. and Luu, J. (2001). *Astron. J.*, 122, 457-473.
- Veillet, C (2001). *IAU Circular No.* 7610 (April 16).
- Weidenschilling, S. (1981). *Icarus*, 46, 124-126.
- Whipple, F. L. (1963). In *The Solar System IV: The Moon, Meteorites, and Comets*. Eds. B. M. Middlehurst and G. J. Kuiper, Univ. Chicago Press, Chicago.
- Yeomans, D. et al. (1997). *Science*, 278, 2106-2109.
- Young, E., Binzel, R., and Crane, K. (2001). *Astron. J.*, 121, 552-561.

Fig. 1.— Sample rotational lightcurve data for Varuna from UT 2001 February 17. Error bars of 0.02 mag. have been plotted for reference.

Fig. 2.— Phase dispersion minimization (PDM) plot computed from the entire R-band data set of Varuna (February 2001 and April 2001 observations). The best fit is the frequency near 3.78 cycles per day (double-peaked period of 6.34 hours). The other large peaks flanking the 3.78 frequency are the 24 hour sampling aliases. The single-peaked period is at 7.57 cycles per day (period of 3.17 hours) with associated flanking 24 hour alias periods.

Fig. 3.— Same as Figure 2 but plotted with the Period as the x-axis and at higher resolution on the single-peaked best fit to show the aliases caused by the ~ 60 day gap between the February 2001 and April 2001 observations. The 3 lower peaks are all reasonable fits to the data, with the middle peak at 3.1721 hours being the best fit for the single-peaked lightcurve.

Fig. 4.— The R-band photometry of Varuna phased according to the double-peaked rotation period $P_{rot} = 6.3442$ hours. The April data has been brightened by 0.09 magnitudes to correct for the dimming effects of a higher phase angle (see Sheppard and Jewitt 2002) and further distance of Varuna compared to the February observations.

Fig. 5.— The B-V, R-I, and V-R colors of Varuna showing no significant variation over its rotation. The R-I colors have been shifted up by 0.5 magnitudes for clarity in distinguishing them from the V-R plotted colors.

Fig. 6.— Porosity, f_v , versus rock fraction, ψ , from Eq. (10). Models for $\bar{\rho} = 1000 \text{ kg m}^{-3}$ and $\bar{\rho} = 1200 \text{ kg m}^{-3}$ are indicated. The upper(lower) line for each density refers to an assumed rock density $\rho_r = 3000(2000) \text{ kg m}^{-3}$. The range of rock fractions inferred for the icy satellites of Saturn and Uranus by Kossacki and Leliwa-Kopystynski (1993) is shown for comparison.

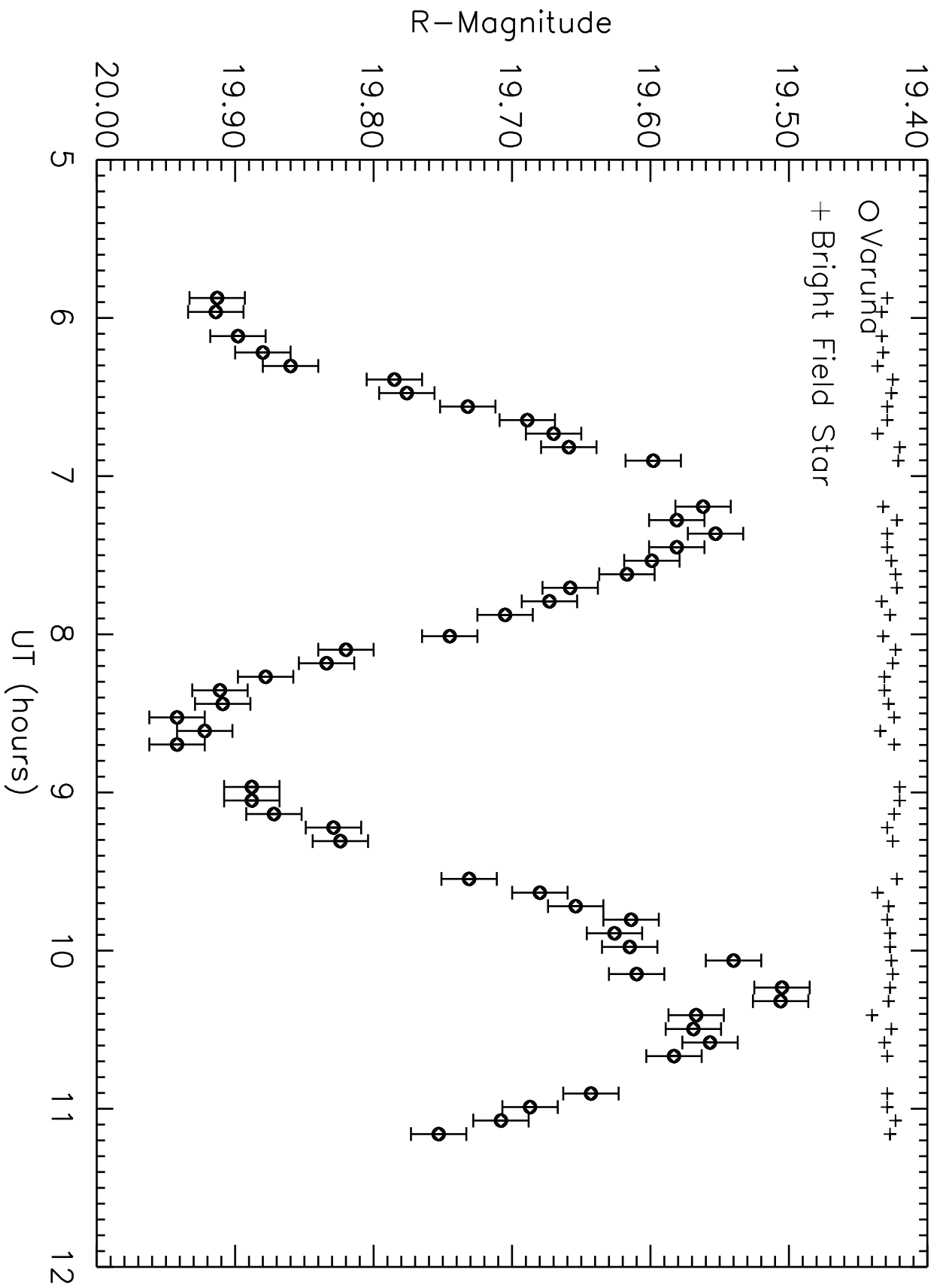


TABLE 1. Journal of Observations for Varuna

UT Date ^a (2001)	JD ^b (2450000+)	Filters ^c	Seeing ^d [arcsec]	R ^e [AU]	Δ ^f [AU]	α ^g [deg]	t_L ^h [min]
Feb 17	1957.5	R	1.1	43.0539	42.4039	0.99	352.6621
Feb 18	1958.5	V,R	0.7	43.0540	42.4171	1.01	352.7725
Feb 19	1959.5	R,B,I	0.6	43.0542	42.4306	1.02	352.8845
Feb 20	1960.5	R	0.7	43.0543	42.4443	1.04	352.9981
Apr 22	2021.5	V,R	0.7	43.0632	43.4447	1.23	361.3187
Apr 24	2023.5	R	0.7	43.0635	43.4764	1.21	361.5823
Apr 25	2024.5	R	0.7	43.0636	43.4921	1.20	361.7126

^aUniversal Time date of the observation

^bCorresponding Julian Date at 0hr UT

^cFilters based on the Johnson-Kron-Cousins system

^dImage FWHM

^eHeliocentric Distance

^fGeocentric Distance

^gPhase angle

^hLight travel time

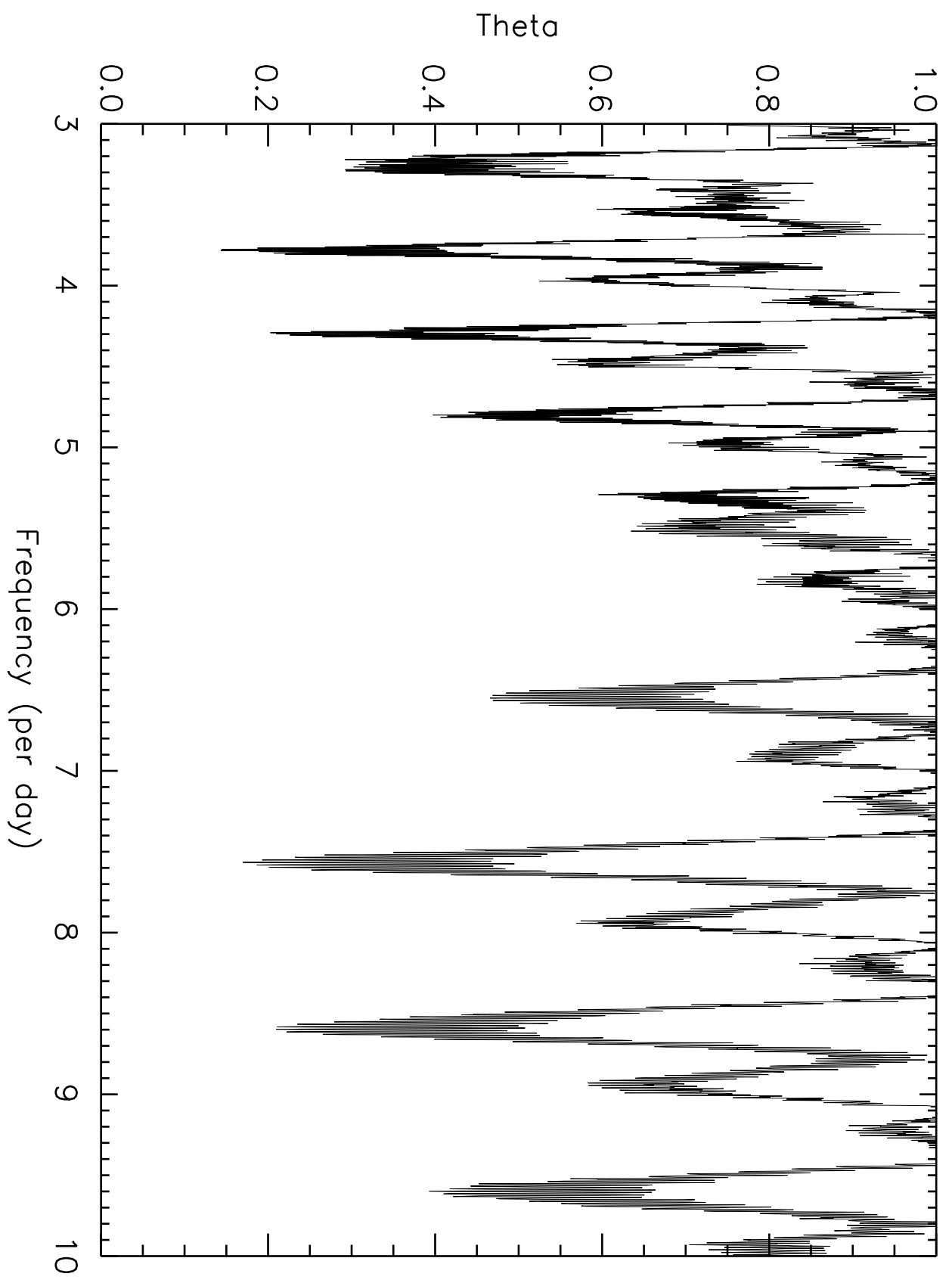


TABLE 2. R-Band Photometry of Varuna

Image ^a	UT Date [2001] ^b	JD _c ^c	m_R ^d	$m_R(1,1,0)$ ^e
2019	Feb 17.2447	1957.49983	19.913	3.450
2020	Feb 17.2484	1957.50464	19.914	3.451
2021	Feb 17.2547	1957.51099	19.898	3.435
2022	Feb 17.2592	1957.51550	19.880	3.417
2023	Feb 17.2627	1957.51904	19.860	3.397
2024	Feb 17.2662	1957.52246	19.785	3.322
2025	Feb 17.2698	1957.52600	19.776	3.313
2026	Feb 17.2733	1957.52954	19.732	3.269
2027	Feb 17.2769	1957.53320	19.689	3.226
2028	Feb 17.2805	1957.53674	19.670	3.207
2029	Feb 17.2840	1957.54028	19.659	3.196
2030	Feb 17.2876	1957.54382	19.598	3.135
2032	Feb 17.2998	1957.55603	19.562	3.099
2033	Feb 17.3033	1957.55957	19.581	3.118
2034	Feb 17.3068	1957.56311	19.553	3.090
2035	Feb 17.3105	1957.56677	19.581	3.118
2036	Feb 17.3140	1957.57019	19.599	3.136
2037	Feb 17.3175	1957.57373	19.617	3.154
2038	Feb 17.3211	1957.57739	19.658	3.195
2039	Feb 17.3247	1957.58093	19.673	3.210
2040	Feb 17.3282	1957.58447	19.705	3.242
2041	Feb 17.3339	1957.59009	19.745	3.282
2042	Feb 17.3374	1957.59363	19.820	3.357
2043	Feb 17.3410	1957.59717	19.834	3.371
2044	Feb 17.3445	1957.60083	19.878	3.415
2045	Feb 17.3481	1957.60437	19.911	3.448
2046	Feb 17.3517	1957.60791	19.909	3.446
2047	Feb 17.3552	1957.61145	19.942	3.479
2048	Feb 17.3588	1957.61499	19.922	3.459
2049	Feb 17.3624	1957.61865	19.942	3.479
2051	Feb 17.3736	1957.62976	19.888	3.425
2052	Feb 17.3771	1957.63342	19.888	3.425
2053	Feb 17.3807	1957.63696	19.872	3.409
2054	Feb 17.3842	1957.64050	19.829	3.366
2055	Feb 17.3878	1957.64404	19.824	3.361
2057	Feb 17.3978	1957.65405	19.731	3.268
2058	Feb 17.4014	1957.65759	19.679	3.217
2059	Feb 17.4050	1957.66125	19.654	3.191
2060	Feb 17.4085	1957.66479	19.614	3.151
2061	Feb 17.4121	1957.66833	19.626	3.163
2062	Feb 17.4157	1957.67200	19.615	3.152
2063	Feb 17.4193	1957.67554	19.540	3.077
2064	Feb 17.4228	1957.67908	19.610	3.147
2065	Feb 17.4264	1957.68262	19.505	3.042
2066	Feb 17.4300	1957.68628	19.506	3.043
2067	Feb 17.4337	1957.68994	19.567	3.104
2068	Feb 17.4373	1957.69360	19.569	3.106
2069	Feb 17.4409	1957.69714	19.557	3.094

TABLE 2. (continued)

Image ^a	UT Date [2001] ^b	JD _c ^c	m_R ^d	$m_R(1,1,0)$ ^e
2070	Feb 17.4445	1957.70081	19.583	3.120
2072	Feb 17.4543	1957.71057	19.643	3.180
2073	Feb 17.4579	1957.71411	19.687	3.224
2074	Feb 17.4614	1957.71765	19.708	3.245
2075	Feb 17.4650	1957.72131	19.753	3.290
3025	Feb 18.2337	1958.48987	19.536	3.071
3026	Feb 18.2396	1958.49585	19.603	3.138
3027	Feb 18.2432	1958.49939	19.613	3.148
3028	Feb 18.2468	1958.50305	19.634	3.169
3029	Feb 18.2503	1958.50647	19.661	3.196
3031	Feb 18.2575	1958.51367	19.758	3.293
3033	Feb 18.2646	1958.52075	19.836	3.371
3035	Feb 18.2718	1958.52795	19.909	3.444
3037	Feb 18.2789	1958.53503	19.939	3.474
3039	Feb 18.2861	1958.54224	19.969	3.504
3049	Feb 18.3223	1958.57849	19.799	3.334
3051	Feb 18.3295	1958.58569	19.731	3.265
3053	Feb 18.3366	1958.59277	19.673	3.208
3055	Feb 18.3439	1958.60010	19.632	3.167
3057	Feb 18.3510	1958.60718	19.581	3.116
3059	Feb 18.3582	1958.61438	19.573	3.108
3074	Feb 18.4277	1958.68384	19.931	3.466
3075	Feb 18.4314	1958.68762	19.955	3.490
3076	Feb 18.4349	1958.69104	19.864	3.399
3077	Feb 18.4385	1958.69470	19.852	3.387
3078	Feb 18.4421	1958.69824	19.833	3.368
3079	Feb 18.4457	1958.70178	19.801	3.336
3080	Feb 18.4492	1958.70532	19.766	3.301
4025	Feb 19.2381	1959.49414	19.835	3.367
4026	Feb 19.2417	1959.49780	19.798	3.330
4027	Feb 19.2452	1959.50134	19.771	3.303
4030	Feb 19.2586	1959.51465	19.628	3.160
4033	Feb 19.2753	1959.53137	19.537	3.069
4036	Feb 19.2883	1959.54443	19.544	3.076
4039	Feb 19.3016	1959.55774	19.625	3.157
4044	Feb 19.3273	1959.58350	19.891	3.423
4047	Feb 19.3405	1959.59656	19.928	3.460
4050	Feb 19.3536	1959.60974	19.951	3.483
4062	Feb 19.4036	1959.65967	19.592	3.124
4065	Feb 19.4167	1959.67285	19.565	3.097
5024	Feb 20.2402	1960.49622	19.754	3.283
5025	Feb 20.2437	1960.49976	19.792	3.321
5026	Feb 20.2473	1960.50330	19.841	3.370
5030	Feb 20.2722	1960.52820	19.961	3.490
5031	Feb 20.2758	1960.53186	19.965	3.494
5032	Feb 20.2794	1960.53540	19.933	3.462
5033	Feb 20.2830	1960.53906	19.915	3.444
5034	Feb 20.2866	1960.54260	19.893	3.422

TABLE 2. (continued)

Image ^a	UT Date [2001] ^b	JD _c ^c	m_R ^d	$m_R(1,1,0)$ ^e
5035	Feb 20.2902	1960.54614	19.849	3.378
5036	Feb 20.2937	1960.54980	19.855	3.384
5041	Feb 20.3273	1960.58337	19.574	3.103
5042	Feb 20.3312	1960.58716	19.565	3.094
5044	Feb 20.3430	1960.59900	19.548	3.077
5045	Feb 20.3468	1960.60278	19.569	3.098
5046	Feb 20.3506	1960.60669	19.583	3.112
5047	Feb 20.3545	1960.61047	19.566	3.095
3022	Apr 22.2417	2021.49219	19.776	3.224
3023	Apr 22.2458	2021.49634	19.746	3.194
3036	Apr 22.2861	2021.53699	19.655	3.103
3038	Apr 22.2958	2021.54663	19.745	3.193
5015	Apr 24.2523	2023.50269	19.615	3.064
5016	Apr 24.2565	2023.50696	19.616	3.065
5021	Apr 24.2853	2023.53564	19.807	3.256
5022	Apr 24.2896	2023.53992	19.857	3.306
6018	Apr 25.2382	2024.48853	20.005	3.455
6019	Apr 25.2425	2024.49280	20.037	3.487
6026	Apr 25.2863	2024.53662	19.718	3.168
6027	Apr 25.2906	2024.54089	19.695	3.145

^aImage number.

^bDecimal Universal Date at the start of the integration.

^cJulian Date corrected to the midpoint of each integration and for light travel time, less 245,0000.

^dApparent red magnitude, uncertainties are ± 0.02 .

^eAbsolute magnitude found using $m_R(1,1,0) = m_R - 5\log(R\Delta) - \beta_{opp}\alpha$ where $\beta_{opp} = 0.156$ magnitudes per degree (see Sheppard and Jewitt 2002).

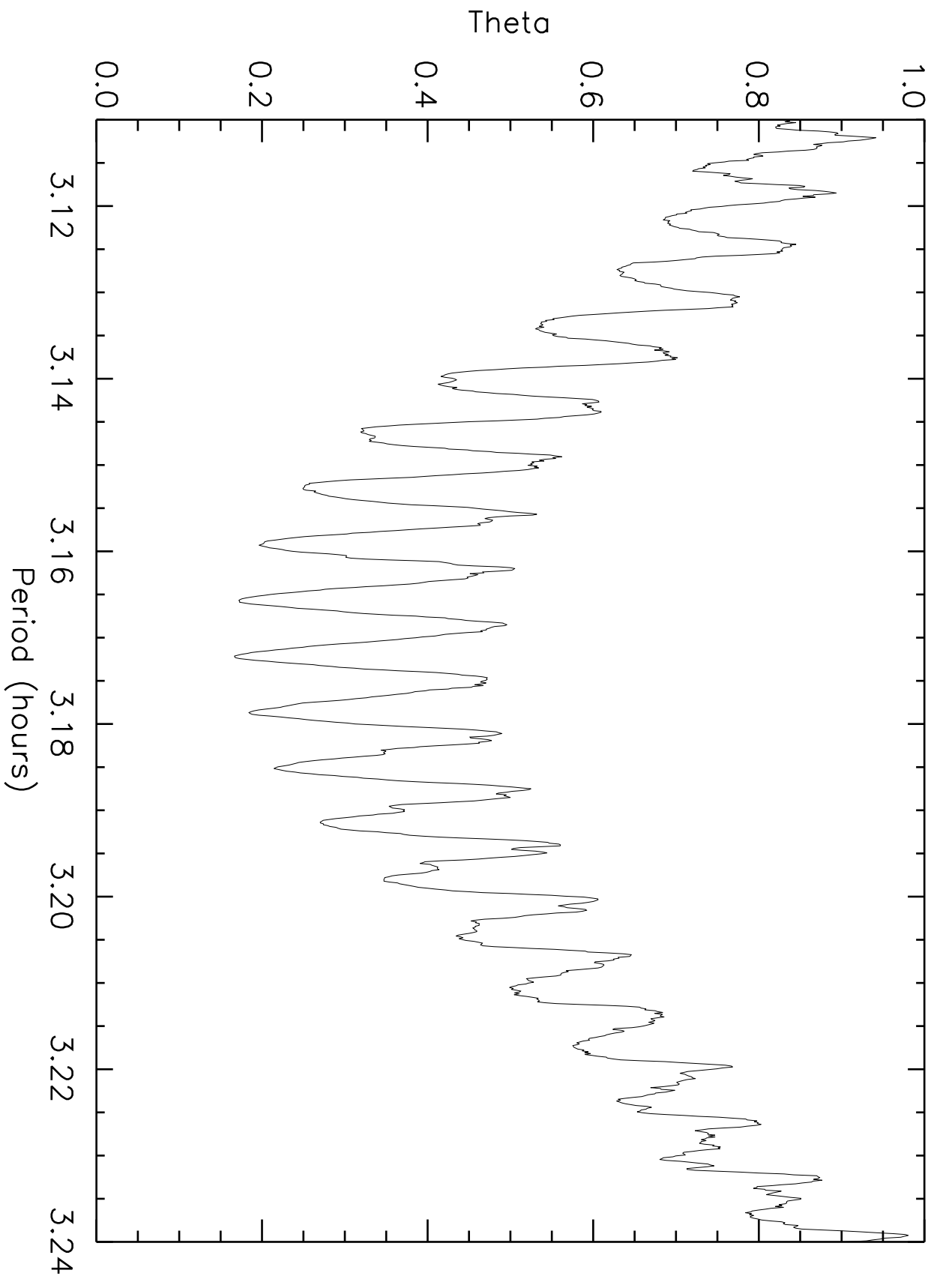


TABLE 3. Color Measurements of Varuna

UT Date	Image	JD _c ^a	Phase ^b	R ^c	B-R	V-R	R-I
2001 Feb 18	3030	1958.5101	0.818	19.71	–	0.63	–
2001 Feb 18	3032	1958.5172	0.845	19.78	–	0.64	–
2001 Feb 18	3034	1958.5244	0.872	19.85	–	0.66	–
2001 Feb 18	3036	1958.5316	0.899	19.91	–	0.69	–
2001 Feb 18	3038	1958.5387	0.926	19.94	–	0.68	–
2001 Feb 18	3050	1958.5786	0.090	19.77	–	0.63	–
2001 Feb 18	3052	1958.5894	0.117	19.71	–	0.62	–
2001 Feb 18	3054	1958.5966	0.144	19.64	–	0.64	–
2001 Feb 18	3056	1958.6038	0.171	19.59	–	0.62	–
2001 Feb 18	3058	1958.6108	0.199	19.56	–	0.64	–
2001 Feb 19	4028	1959.5052	0.583	19.72	–	–	0.63
2001 Feb 19	4029	1959.5099	0.596	19.69	1.48	–	–
2001 Feb 19	4031	1959.5183	0.632	19.61	–	–	0.64
2001 Feb 19	4032	1959.5266	0.659	19.57	1.49	–	–
2001 Feb 19	4034	1959.5349	0.695	19.54	–	–	0.61
2001 Feb 19	4035	1959.5396	0.708	19.54	1.50	–	–
2001 Feb 19	4037	1959.5480	0.744	19.56	–	–	0.61
2001 Feb 19	4038	1959.5530	0.758	19.58	1.48	–	–
2001 Feb 19	4040	1959.5612	0.795	19.65	–	–	0.65
2001 Feb 19	4041	1959.5663	0.809	19.69	1.51	–	–
2001 Feb 19	4045	1959.5870	0.892	19.89	–	–	0.59
2001 Feb 19	4046	1959.5917	0.905	19.92	1.48	–	–
2001 Feb 19	4048	1959.6001	0.941	19.95	–	–	0.61
2001 Feb 19	4049	1959.6047	0.955	19.96	1.48	–	–
2001 Feb 19	4051	1959.6132	0.991	19.95	–	–	0.63
2001 Feb 19	4052	1959.6179	0.005	19.94	1.49	–	–
2001 Feb 19	4063	1959.6632	0.180	19.58	–	–	0.60
2001 Feb 19	4064	1959.6680	0.194	19.57	1.49	–	–
2001 Feb 19	4066	1959.6777	0.240	19.57	–	–	0.61
2001 Feb 19	4067	1959.6812	0.253	19.58	1.52	–	–
2001 Apr 22	3024	2021.5009	0.139	19.66	–	0.64	–
2001 Apr 22	3025	2021.5057	0.157	19.62	–	0.62	–
2001 Apr 22	3035	2021.5303	0.257	19.58	–	0.64	–
2001 Apr 22	3037	2021.5420	0.294	19.66	–	0.64	–
MEAN					1.49 ± 0.01	0.64 ± 0.01	0.62 ± 0.01

^aJulian day at mid-exposure and corrected for light travel time, less 245,0000.

^bRotational phase of Varuna lightcurve with period 6.34 hours. The phase corresponds to Figure 4 where 0.45 and 0.95 are minimum light (~ 19.9) and 0.20 and 0.70 are maximum light (~ 19.5) of the double-peaked lightcurve.

^cR magnitude interpolated to the time of the corresponding BVI data.

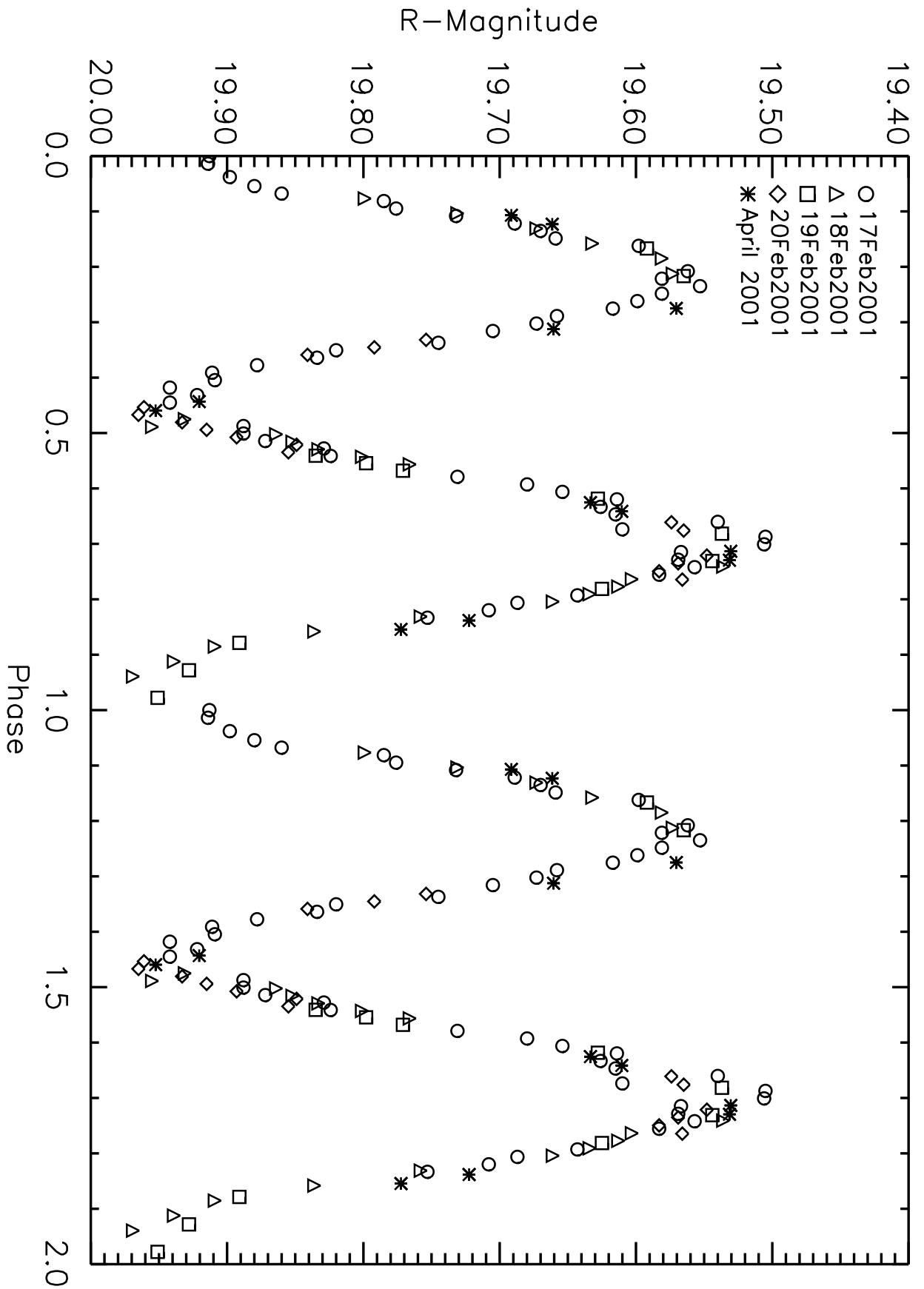


TABLE 4. Comparison of Rotational Color Variations

Object	Δm [mag.]	$\Delta m(\text{B-V})$ [mag.]	Reference
Varuna	0.42 ± 0.02	< 0.02	This Work
Iapetus	~ 2	$0.07 - 0.10$	Millis (1977)
Pluto	0.35	0.01	Buie, Tholen and Wasserman (1997)

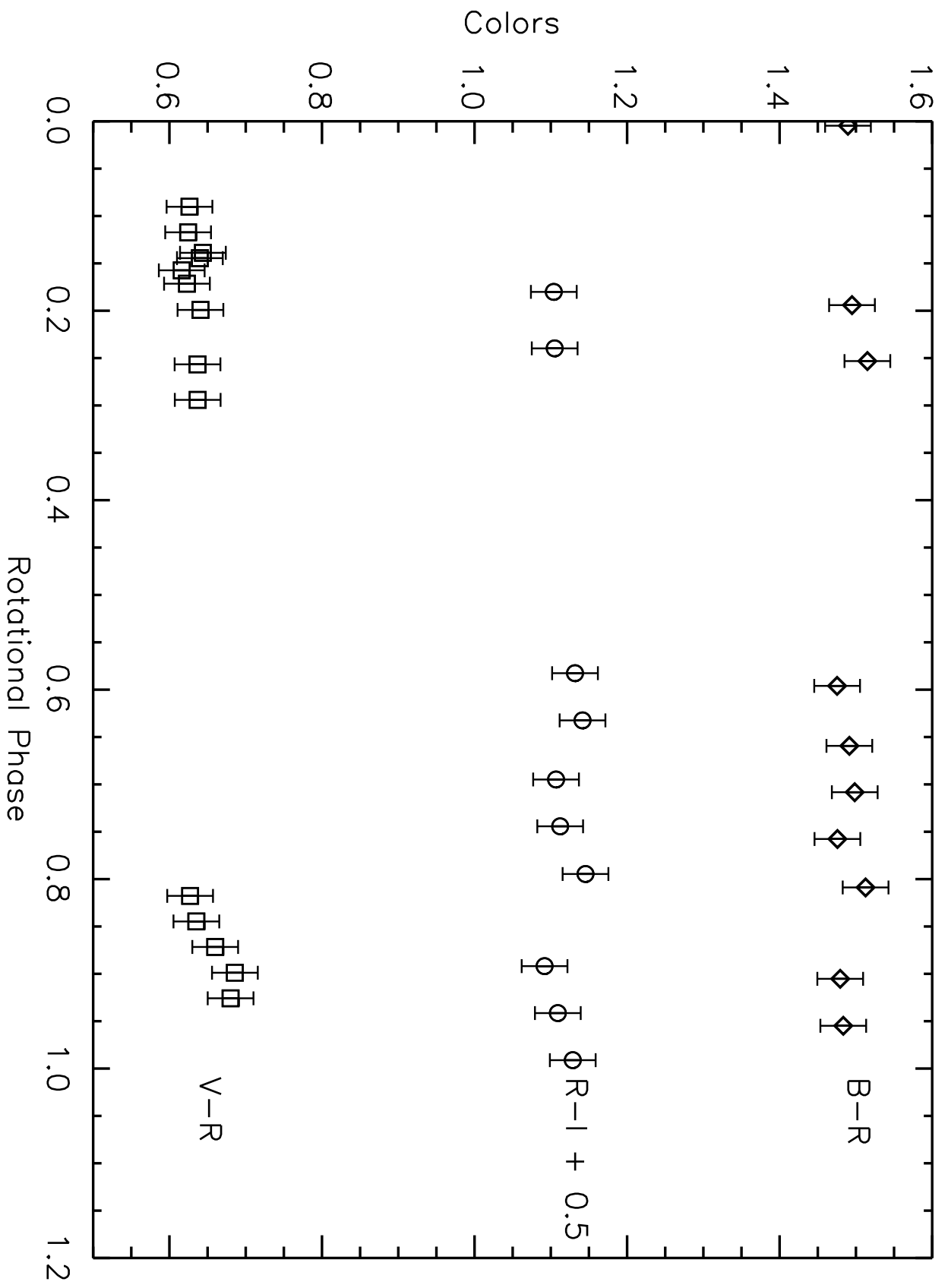


TABLE 5. Shape Models and Density For Varuna

Model	Shape	Axis Ratios ^a	Density [kg m ⁻³]
Albedo Spots	Sphere	1:1:1	≥ 1090
Jacobi	Ellipsoid	≥1.5:1.0:0.7	≥ 1050
Binary	Contact Spheres	≥1.4:1	≥ 996
Binary	Roche Ellipsoids	1.06:1, 1.67:1	3600

^aFor the binary models, the listed "axis ratio" is the ratio of the diameters of the separate components

